

A multiwavelength view of the protostellar binary IRAS04325+2402: a case for turbulent fragmentation

A. Scholz^{1,2*}, K. Wood², D. Wilner³, R. Jayawardhana⁴, P. Delorme²,
A. Caratti o Garatti¹, V. D. Ivanov⁵, I. Saviane⁵, B. Whitney⁶

¹ *School of Cosmic Physics, Dublin Institute for Advanced Studies, 31 Fitzwilliam Place, Dublin 2, Ireland*

² *SUPA, School of Physics & Astronomy, University of St. Andrews, North Haugh, St. Andrews, Fife KY16 9SS, United Kingdom*

³ *Harvard-Smithsonian Center for Astrophysics, 60 Garden St., MS 42, Cambridge, MA 02138, USA*

⁴ *Department of Astronomy & Astrophysics, University of Toronto, 50 St. George Street Toronto, ON M5S 3H4, Canada*

⁵ *European Southern Observatory, Ave. Alonso de Cordova 3107, Casilla 19, Santiago 19001, Chile*

⁶ *Space Science Institute, 4750 Walnut St. Suite 205, Boulder, CO 80301, USA*

Accepted. Received.

ABSTRACT

IRAS04325+2402 (hereafter IRAS04325) is a complex protostellar system hosting two young stellar objects (AB and C in the following) at a separation of 1250 AU. Here we present new deep Gemini imaging and spectroscopy for the system covering the wavelength regime from 1-12 μm as well as Sub-Millimeter Array interferometry at 870 μm , in combination with Spitzer and literature data. Based on this rich dataset we provide a comprehensive picture of IRAS04325 over scales from a few AU to several parsec. Object AB is a low-mass star with a disk/envelope system and an outflow cavity, which is prominently seen in infrared images. Object C, previously suspected to be a brown dwarf, is likely a very low mass star, with an effective temperature of $\sim 3400\text{K}$. It features an edge-on disk and an elongated envelope, and shows strong indications for accretion and ejection activity. Both objects are likely to drive parsec-scale molecular outflows. The two objects are embedded in an isolated, dense molecular cloud core. High extinction, lack of X-ray emission, and relatively high bolometric luminosity argue for a very young age below 1 Myr. The disk/outflow systems of AB and C are misaligned by ~ 60 deg against each other and by 80 and 40 deg against the orbital plane of the binary. The system might be a good case for primordial misalignment, as opposed to misalignment caused by dynamical interactions, because the outflow direction is constant and the realignment timescale is likely larger than the system age. This favours turbulent fragmentation, rather than rotational fragmentation, as the formation scenario. We show that the spectral energy distributions and images for the two objects can be reproduced with radiative transfer models for disk/envelope systems. Our analysis provides reassurance in the established paradigm for the structure and early evolution of YSOs, but stresses the importance of developing 3D models with sophisticated dust chemistry.

Key words: stars: low-mass, brown dwarfs, stars: circumstellar matter, stars: pre-main sequence, stars: formation

1 INTRODUCTION

The study of protostars and their environment requires the analysis of radiation across a broad range of wavelengths, including the infrared and the submm/mm regime. At the same time, it is desirable to achieve high spatial resolution to characterize the small-scale structures close to the sources (see review by Watson et al. 2007). However, only a few ob-

jects have been studied at uniform and high resolution over the full wavelength domain of relevance (1-1000 μm). Testing the current paradigms for collapse, accretion/outflow, and disk evolution with high-resolution multi-wavelength studies of individual objects is thus of major importance.

In this paper we present a case study for the protostellar system IRAS04325+2402 (hereafter: IRAS04325), shown in Fig. 1. Originally identified as LDN 1535 in the catalogue of dark clouds by Lynds (1962), it has been studied extensively over three decades (117 publications according to SIMBAD).

* E-mail: aleks@cp.dias.ie

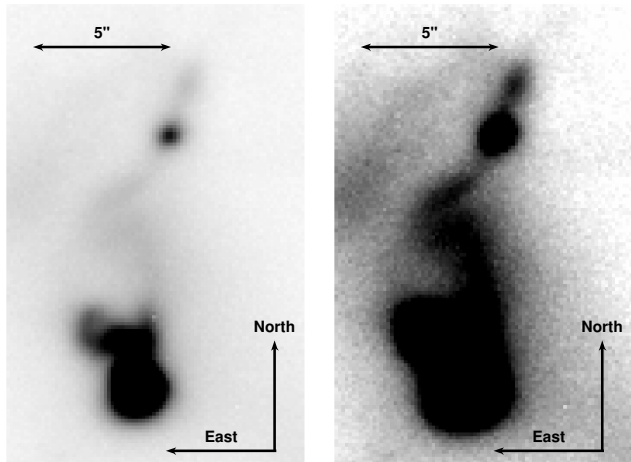


Figure 1. K-band close-up view of IRAS04325 obtained with Gemini-North and NIRI. The image is shown in two different intensity scales: the left panel shows the point sources and bright extended emission close to the southern source AB, and the right panel illustrates the faint structure between AB and the northern source C.

A number of publications starting in the 1980s has focused on the molecular gas in L1535 and the large-scale environment (e.g. Ungerechts et al. 1982; Goldsmith & Sernyak 1984). After the identification of an IRAS source associated with this cloud (Parker 1988, 1991), the object has been analysed in the infrared domain (e.g. Hodapp 1994) and in the submm/mm continuum (e.g. Ladd et al. 1991; Ohashi et al. 1996; Saraceno et al. 1996), tracing the dust in the system. IRAS04325 was found to harbour a protostar with subsolar luminosity and a disk seen at high inclination (Kenyon et al. 1993a,b), embedded in a cloud core with a diameter of several tens of thousands of AU. In addition, large-scale outflow activity has been identified (e.g. Heyer et al. 1987; Moriarty-Schieven et al. 1992; Wang et al. 2001). The source is established as a prototypical small-scale site of star formation.

Until 1999, the structures within the IRAS beam have not been resolved, which results in various problems. The near-infrared images clearly show a bright nebulosity, indicating that the fluxes from IRAS and single-dish observations are contaminated by extended emission. As a result the properties of the central source and its close environment are poorly constrained. Confusingly, the direction of one of the large-scale outflows does not agree with the orientation of the infrared nebulosity, interpreted as outflow cavity, as pointed out by Kenyon et al. (1993a). Hartmann et al. (1999) presented HST imaging of the object, revealing complex substructure. In particular, the images show the presence of a second well-separated point source (IRAS04325C), which has a resolved disk seen edge-on. The main light source IRAS04325AB is speculated to be a binary. In addition there are various scattered light features.

Originally fueled by the suspicion the second source IRAS04325C might be a proto brown dwarf, we have conducted our own observations of the system. In our first paper (Scholz et al. 2008), we detect the second component with 1.3 mm interferometry and show the first infrared spectrum

for this object. Here we present a comprehensive dataset for the full IRAS04325 system, including new near- and mid-infrared imaging, near-infrared spectroscopy for both components, and submillimeter interferometry. We consistently assume a distance of 150 pc for the Taurus star forming region (Loinard et al. 2007) when converting from apparent to physical separations. All physical distances are given in projection against the plane of the sky and should be seen as lower limits to the actual distances.

2 OBSERVATIONS AND DATA REDUCTION

2.1 Near-infrared imaging

Near-infrared images in J-, H-, and K'-band were taken on the 23 August 2008 with the NIRI camera (Hodapp et al. 2003) at the Gemini-North 8.1 m telescope¹. All Gemini observations for IRAS04325 were taken in queue mode in the band-2 program GN-2008B-Q-73. We used the f/6 camera with a scale of $0''.12/\text{pix}$ and $120'' \times 120''$ FOV. A 7-step dither pattern was carried out in each band with $15''$ offsets and 10 sec integration time per position. The total on-source time in each band was 70 sec. The seeing measured from 1-3 well-detected point sources outside IRAS04325 was $0''.5$.

The reduction of the NIRI J-, H- and K'-band images proceeded as follows: a sky image for each filter was created using the dithered science images. The sky was then subtracted to each science image using the ESO eclipse package (Devillard 1997). We carried out a flatfield correction using domeflats. The alignment and coaddition of the images was done with the programs Scamp (Bertin 2006) and Swarp (Bertin et al. 2002) to produce the final science stacks.

In the same Gemini program, we obtained L'- ($3.8 \mu\text{m}$) and M'-band ($4.7 \mu\text{m}$) images with NIRI's f/32 camera ($0''.02/\text{pix}$) and a FOV of $22.4'' \times 22.4''$. In the L-band a five step dither pattern with $3''$ offsets was executed twice with 20 coadded 1 sec exposures at each position, which gives a total on-source time of 200 sec. The same pattern was carried out 13 times in the M-band with 30 coadded 0.5 sec exposures, in total 25 min. These observations were obtained on the 3rd of December 2008, including a set of images for the bright A0 star HD36719 for calibration purposes. All data was taken at low airmass (< 1.2); the airmass difference between science and calibration target was $\lesssim 0.1$.

For the reduction of the L- and M-band data we followed the standard recipes based on the tools in the Gemini/NIRI package within IRAF. Flats and sky images were created based on the dithered science images, discarding the first frame. In the L-band all nine available images were used for the sky frame. The M-band sequence is long enough for the sky to change significantly. For each individual frame we used the nine frames taken closest in time to create

¹ The Gemini Observatory is operated by the Association of Universities for Research in Astronomy, Inc., under a cooperative agreement with the NSF on behalf of the Gemini partnership: the National Science Foundation (United States), the Science and Technology Facilities Council (United Kingdom), the National Research Council (Canada), CONICYT (Chile), the Australian Research Council (Australia), Ministério da Ciência e Tecnologia (Brazil) and Ministerio de Ciencia, Tecnología e Innovación Productiva (Argentina)

the sky image. After subtracting the sky the science frames were divided by the normalized flatfield. The resulting images were mostly flat with the exception of the first and last two frames in the M-band suffering from imperfect sky subtraction. These images with uneven background were discarded. To coadd the individual images we used the standard `combine` routine in IRAF. The images of the standard star for L- and M-band were handled in exactly the same way.

2.2 Mid-infrared imaging

IRAS04325 was observed with Gemini-North and Michelle (Bryson et al. 1994) in the N'-band with a central wavelength of $11.2\ \mu\text{m}$ on the 3rd of November 2008. To sample the sky properly the standard procedure including chopping and nodding was used. In short, the pointing was chopped at 4.2 Hz between the target and an adjacent position $15''$ to the east by moving the secondary mirror. In addition the whole telescope was nodded in the same direction in larger time intervals. The chop throw was chosen to avoid the extended emission from IRAS04325 from the sky field. The exposure time per frame was 0.02 sec; in total we integrated 2×590 sec on source. The airmass for the two science integrations was 1.07 and 1.02. In addition, the standard star HD20893 was observed at airmass 1.02.

For the standard reduction we used the Gemini/MIDIR package in IRAF and followed the 'cookbook' for Michelle provided by Gemini. This includes the tasks `miregister` to prepare and reformat the data cubes and `mistack` to average by coadding the signal from each nod position and dividing by the number of frames. A residual pattern was removed by fitting each column with a constant and subtracting this fit. Source C is weakly visible only in one of the resulting stacked frames – the one taken at lower airmass. The peak intensity for object C is about three times the noise in the sky background. The signal does not improve significantly when coadding the two images. Only the image with detection was used for the photometry. The standard star frames were reduced in the same fashion as the science images.

2.3 Near-infrared spectroscopy

Object AB was observed with SofI (Morwood 1997) in spectroscopy mode at the ESO/NTT in La Silla. We obtained this spectrum and the associated calibration files from the ESO archive. The low-resolution Red Grism was used with coverage from 1.5 to $2.5\ \mu\text{m}$ and a $0''.6$ slit, which results in a resolution of $R \sim 1000$. Two pairs of nodded integrations (ABBA) were observed with a nodding step of $20''$ and 225 sec exposure time per position. The total on-source time was 900 sec. A telluric standard star (HIP 23719, spectral type G1V) was observed immediately after the science target.

We carried out a standard reduction, including subtraction of the nodded pairs (A-B) to remove the sky and flat-field correction. The four spectra were extracted with a $1''.2$ aperture, wavelength calibrated using Xenon arc spectra, and coadded. The telluric spectrum was treated in the same way. The combined spectrum for IRAS04325AB was then divided by the telluric spectrum and multiplied by the solar spectrum. The final science spectrum is shown in Fig. 4.

We obtained a spectrum for object C on Oct 14/15 2008 with Gemini-North and NIRI, using the f/6 camera, the 6-pix slit mask (slit width $0''.72$) and the H- and K-band grisms. This gave a resolution of $R \sim 500$ over a wavelength range of 1.4 - $2.5\ \mu\text{m}$. The slit was aligned in E-W direction. The total on-source time of 3000 sec per band was split in 10 single integrations. To correct for the variable background emission, the object was moved along the slit in steps of $2''$ between the single exposures. For telluric correction we observed the early A stars HIP17791 and HIP23088 in the same observing nights.

The NIRI spectra were extracted and calibrated using our own IDL procedures. The frames were flat fielded using an internal flat taken immediately after the science frames. Consecutive exposures are subtracted to remove the sky background. The 10 individual spectra are then extracted and median-combined. The same operation is performed for the telluric calibration stars. From the standard spectra we derived a telluric spectrum by dividing through a black body spectrum with a temperature of 10000 K and interpolating over the hydrogen lines. The science spectrum was divided by the telluric spectrum. The wavelength calibration was carried out based on the bright OH lines which are visible in the (unreduced) science images. The final H- and K-band spectra are shown in Fig. 5.

2.4 Archival images

To complement our dataset, we used archival images for the Taurus region. Our target and its environment is covered by the TAP Survey, carried out with the near-infrared camera WFCAM at the United Kingdom Infrared Telescope² (Davis et al. 2008). The survey provides a database of near-infrared images in the K-band and the narrow-band filter centered on the 1-0 S(1) hydrogen emission feature at $2.122\ \mu\text{m}$ (in the following called: H₂ band), which we use to look for shocked emission caused by molecular outflows.

In addition, we downloaded the pipeline-reduced PBCD Spitzer images from the 3rd delivery (DR3) of the Taurus Spitzer Legacy project (PI: Deborah Padgett, program id #3584) from the NASA/IPAC Infrared Science Archive. This includes the IRAC data in the four channels at 3.6, 4.5, 5.8 and $8.0\ \mu\text{m}$, as well as the MIPS images at 24 and $70\ \mu\text{m}$.

2.5 Submillimeter interferometry

A field centered on IRAS04325 was observed with the SMA³ on 20 October 2008 using eight antennas in a compact configuration that provided baseline lengths of 11 to 77 m. The weather was good, with system temperatures of 200 to 250 K (DSB) near transit. The phase center was RA $04^{\text{h}}35^{\text{m}}35^{\text{s}}.29$, DEC $+24^{\circ}08'27''.6$ (J2000), which is the position of IRAS04325C. The correlator was configured for

² The TAP survey is hosted by the Joint Astronomy Center. Image reduction was carried out by the Cambridge Astronomical Survey Unit for the WFCAM Science Archive. For more information, see <http://www.jach.hawaii.edu/UKIRT/TAP/>.

³ The Submillimeter Array is a joint project between the Smithsonian Astrophysical Observatory and the Academia Sinica Institute of Astronomy and Astrophysics and is funded by the Smithsonian Institution and the Academia Sinica.

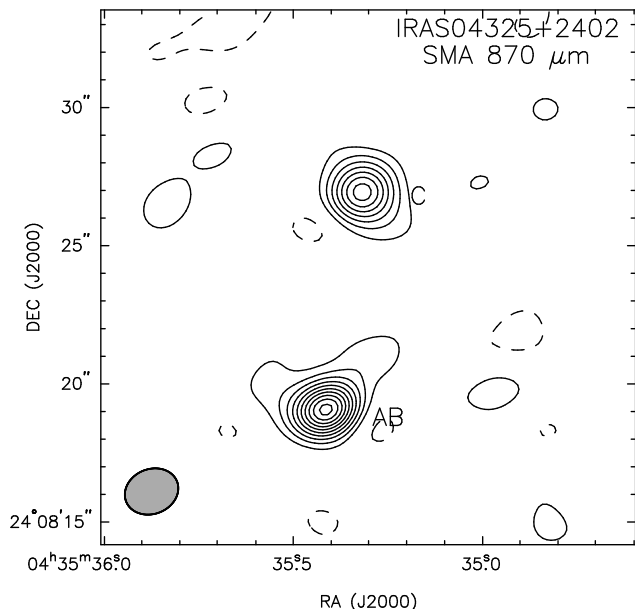


Figure 2. SMA 870 μm dust continuum image showing the two sources AB and C and associated extended emission. The ellipse in the lower left corner shows the $2''.0 \times 1''.6$ PA -68 deg beam. The lowest contour and step are 4.4 mJy/beam (twice the rms noise level). Negative contours are dashed.

the full 2 GHz bandwidth, including one spectral chunk of 82 MHz in the middle of the upper sideband devoted to the CO J=3-2 line at 345.786 GHz with channel spacing 0.20 MHz (0.176 km s^{-1}). The SMA primary beam FWHM is $35''$ at this frequency. Calibration of complex gains was performed by interleaving 3 minute observations of the quasars 3C111 (4.30 Jy) and J0530+135 (0.84 Jy) with 15 minute observations of IRAS04325 over the hour angle range -5 to $+5$. The flux scale was set using observations of Uranus, with an estimated uncertainty better than 20%. The passband was calibrated using observations of the strong sources 3C454.3 and Uranus. The data calibration was done with the MIR/IDL software, followed by standard imaging and deconvolution tasks within the Miriad package. For the continuum image, the beam size (robust=0) was $2''.0 \times 1''.6$ at PA -68 deg, and the rms noise 2.2 mJy/beam, after combining the lower and upper sidebands (effective bandwidth ~ 4 GHz). For the CO line images, the beam size (natural weight) was $2''.1 \times 1''.8$ at PA -56 deg, with rms noise 0.26 Jy/beam in each spectral channel. The continuum image is shown in Fig. 2; the CO line maps for a sequence of velocity bins are plotted in Fig. 3. Since the interferometer observations are sensitive only to small scale structure ($\lesssim 10''$), the sources seen in the CO maps are not isolated and should be seen as local overdensities and temperature enhancements.

3 QUANTITATIVE ANALYSIS

3.1 Object AB: NIR spectroscopy

The spectrum of the source AB is red and entirely featureless (see Fig. 4), without the broad water absorption bands usually seen in late-type objects (Cushing et al. 2005). The

slope from 1.5 to $2.3 \mu\text{m}$ is well approximated by a straight line. There may be a hint of CO absorption bands at $> 2.3 \mu\text{m}$.

The lack of features precludes a detailed spectral analysis. Instead we simply compare the slope with reddened spectra for late-type objects from the IRTF/SpeX Spectral Library (Rayner et al. 2009). G-, K- and early M-type spectra reddened with $A_V \sim 30$ provide a good match. As an example we show in Fig. 4 the spectrum for the K7V star HD237903. Towards mid-M spectral types the fit becomes progressively worse, no matter which extinction is chosen. In particular, the slope over H- and K-band is no longer constant, due to the water absorption feature between the two bands. In addition, the CO bands and water absorption cause the flux level to drop at $> 2.2 \mu\text{m}$. The mismatch is shown in Fig. 4 where we compare with the spectrum of the M4V star G1299 reddened with $A_V = 30$ mag. Thus, a spectral type later than early M seems unlikely.

This limit on the spectral type, however, needs confirmation, particularly because the spectrum may be affected by additional continuum emission from the disk or accretion. The slit orientation in E-W direction avoids the scattered light features north and south of the source (see Fig. 7), but veiling from the inner disk (within $0''.5$) cannot be excluded. Lacking high-resolution spectroscopy, we cannot put limits on the veiling. Typical excess continuum in T Tauri stars makes the near-infrared spectrum redder (Folha & Emerson 1999), i.e. the spectral type may be earlier than estimated or the extinction may be overestimated.

3.2 Object C: NIR spectroscopy

The spectrum of object C shows features of the photosphere, in particular a flattening at the red end of the H-band and a triangular shape in the K-band (Fig. 5). The spectra in H- and K-band were compared separately to model spectra. We neglect that the spectra might be affected by scattering and veiling. Both effects are expected to be smoothly and slowly varying functions of wavelength, thus they should not affect the spectrum in individual bands significantly.

For the comparison we used a series of AMES-DUSTY model spectra (Allard et al. 2001) with effective temperatures ranging from 2000 to 4000 K and $\log g = 3.5$ or 4.0, as expected for young stars. We varied T_{eff} and A_V and aimed to obtain a consistent solution for the two bands. We find a decent match between observed and model spectra for $T_{\text{eff}} = 3400 \pm 200$ K and extinction $A_V = 22 \pm 2$ mag. As seen in Fig. 5 this fits H and K bands equally well.

It is impossible to match the observed spectrum with a model for an object close or below the substellar boundary ($T_{\text{eff}} \lesssim 3000$ K), as claimed by Scholz et al. (2008), particularly not in the H-band. Young brown dwarfs exhibit a characteristic triangular shaped H-band spectrum due to water absorption (Kirkpatrick et al. 2006; Brandeker et al. 2006; Scholz et al. 2009) which is not seen in our data. We conclude that IRAS04325C is unlikely to be a brown dwarf; its spectrum is more consistent with being a very low-mass star with an effective temperature around 3400 K or spectral type of M3-M4 (Mentuch et al. 2008).

Various emission features associated with molecular hydrogen are clearly detected in the K-band, particularly 1-0 S(2) at 2.034, 1-0 S(1) at 2.122, 1-0 S(0) at 2.223, 1-0 Q(1) at

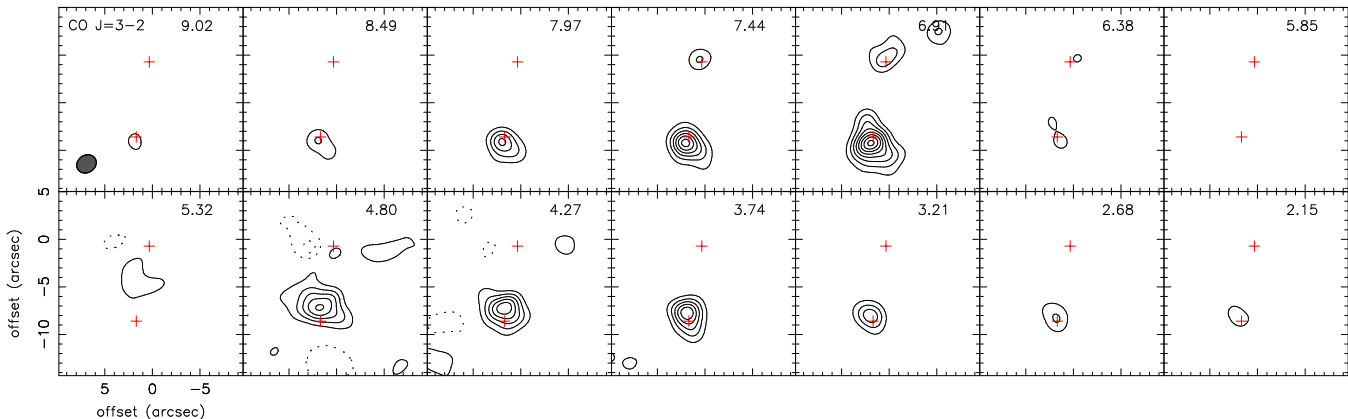


Figure 3. Contour maps of the continuum-subtracted CO line observations with SMA. The contours are in steps of 1.5 Jy/beam, negative contours are dashed. The LSR velocity in km s^{-1} is indicated for each panel. The positions of the compact sources AB and C, as measured in the continuum map, are marked with crosses.

2.407, and 1-0 Q(3) at $2.424 \mu\text{m}$. In addition, there is a Br γ emission feature at $2.166 \mu\text{m}$, commonly associated with ongoing accretion (e.g. Natta et al. 2006). The H-band shows the [FeII] lines at 1.644 , 1.669 , 1.677 , and $1.748 \mu\text{m}$ (the latter might be blended with a hydrogen feature). While the lines of molecular hydrogen can originate in the disk or in a jet, the [FeII] emission can only occur in the jet. Thus, our spectra prove ongoing accretion and outflow activity in IRAS04325C. From the way we have analysed the spectra it is certain that the emission originates in an area within the PSF of the point source, i.e. within a radius of $0''.5$ (75 AU) around the source.

The [FeII] lines provide a constraint on the electron density n_e in the jet (e.g. Nisini et al. 2002; Garcia Lopez et al. 2008). The flux ratio between the well-detected lines at 1.644 and $1.677 \mu\text{m}$ is 2.9, which gives $n_e > 10^5 \text{ cm}^{-3}$. Note that the [FeII] line ratio saturates for larger densities. Consistently, the lower limits to the flux ratios of 1.544 vs. $1.644 \mu\text{m}$ and 1.600 vs. $1.644 \mu\text{m}$ yield densities $> 0.5 \cdot 10^5$ and $> 10^4 \text{ cm}^{-3}$, respectively. Such high values are usually found at the base of the jet, while the density typically drops further away from the source (e.g. Takami et al. 2006; Garcia Lopez et al. 2008). Thus the analysis confirms that the [FeII] emission originates in a jet close to IRAS04325C.

The Br γ line is used to derive an estimate for the mass accretion rate following Natta et al. (2006). The approximate equivalent width in this line is $7 \pm 2 \text{ \AA}$. Scaling with the K-band magnitude of 8.5 mag for a 3400 K star at 1 Myr from Baraffe et al. (1998) gives a line luminosity of $\log(L_{\text{Br}\gamma}/L_{\odot}) \sim -4.1$. With the empirical relations by Calvet et al. (2004) this translates into an accretion luminosity of $\log(L_{\text{acc}}/L_{\odot}) \sim -0.8$ (see also Muzerolle et al. 1998). The mass accretion rate is then $\dot{M} = L_{\text{acc}}R/GM$. Assuming a mass of $0.4 M_{\odot}$ and a radius of $1.5 R_{\odot}$ results in an accretion rate in the range of $(1.0 \pm 0.3) \cdot 10^{-8} M_{\odot} \text{ yr}^{-1}$, comparable to accretion rates derived for T Tauri stars but higher than those for young brown dwarfs (Mohanty et al. 2005).

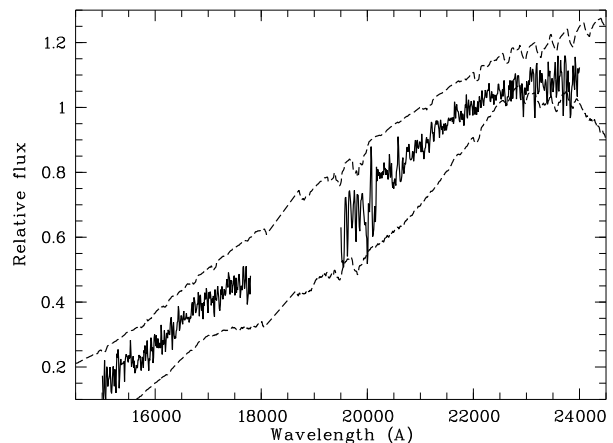


Figure 4. Spectrum for AB obtained with NTT/SOFI. Overplotted with dashed lines are the spectra for a K7V star (above) and a M4V star (below the science spectrum), from the IRTF/SpEx Spectral Library (Rayner et al. 2009). Both comparison spectra are reddened with $A_V = 30 \text{ mag}$.

3.3 Photometry of point sources

We derived magnitudes/fluxes for the two components of IRAS04325 from the Gemini near- and mid-infrared images as well as from the submm continuum map.

For the JHK images we adopted an aperture of $1''.2$ (10 pixel) and a background annulus between $1''.2$ and $1''.8$ (10-15 pixel). The field contains one 2MASS source outside IRAS04325 with $J = 17.98$, $H = 16.41$, and $K = 14.64$ which was used to shift the instrumental magnitudes into the 2MASS system. The resulting values are listed in Table 1. In the J-band there is diffuse emission at the position of object C, but no clear point source; we consider the flux measurement to be an upper limit. The previously published photometry of IRAS04325 has been obtained with larger apertures (Hartmann et al. 1999; Connelley et al. 2008). Hence, these literature fluxes are significantly larger than ours because they include extended emission.

For the L⁻, M⁻, and N⁻-band photometry we used apertures of $1''.0$ or $1''.2$ and a sky annulus similar to the one for

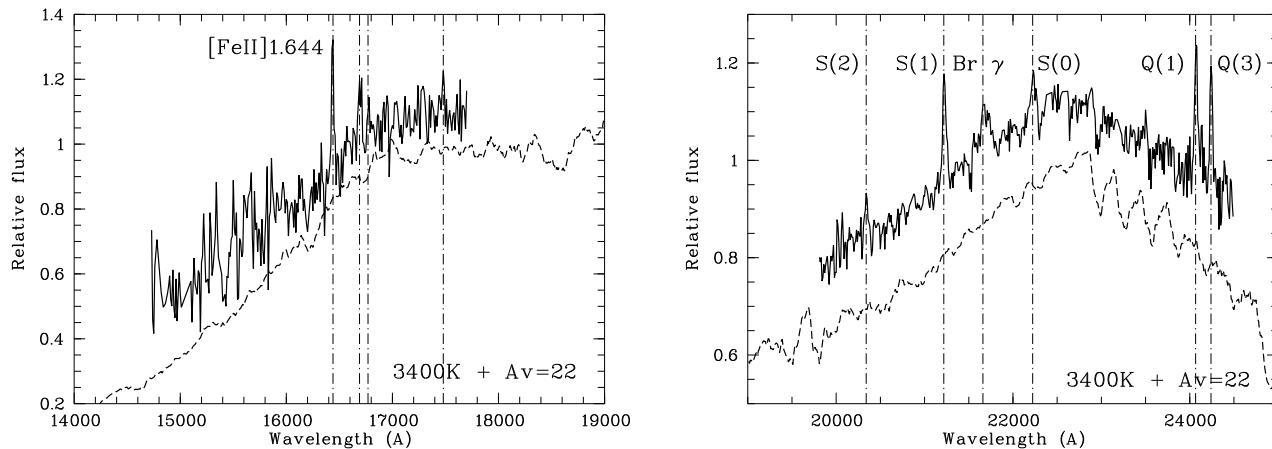


Figure 5. H- and K-band spectrum from Gemini/NIRI (solid line) in comparison with a model (DUSTY, 3400 K, $\log g = 4.0$, $A_V = 22$ mag, see Allard et al. (2001)). The model (dashed line) is shifted in y-direction for clarity. The emission lines detected on the 3σ level are marked with dashdotted lines (see text for more information).

Table 1. IR photometry for the point sources in IRAS04325. If not specified, the uncertainty in the fluxes is $\sim 10\%$; this includes the calibration error. For more details see Sect. 3.3. The fluxes at $1300 \mu\text{m}$ are from Scholz et al. (2008).

Band	λ (μm)	AB	C	unit	aperture ($''$)
J	1.25	16.54	< 18.6	mag	1.2
H	1.65	14.37	16.92	mag	1.2
K'	2.15	11.87	14.75	mag	1.2
L'	3.78	10.36	13.4 ± 0.2	mag	1.0
M'	4.68	9.37	12.3 ± 0.4	mag	1.0
N'	11.2	65	3.4 ± 1.1	mJy	1.2
	870	55	41	mJy	3.0
	1300	10 ± 3	10 ± 3	mJy	2.0

JHK. In these bands the extended emission is less problematic, thus the choice of the sky annulus does not significantly affect the results. The L'/M'-band magnitudes were shifted to the standard system based on the values for the calibration star HD36719, which has 5.4 mag throughout this wavelength regime (Leggett et al. 2003). For the N'-band magnitudes we used the star HD20893 for calibration, for which an N'-band flux of 4.3 Jy is reported on the Gemini website⁴, based on Cohen et al. (1999).

The fluxes in the $870 \mu\text{m}$ continuum map, measured within a $3''.0$ aperture, are 55 and 41 mJy, for AB and C respectively.

The uncertainties were estimated by varying the size of the aperture and the sky annulus and checking the changes in the fluxes. Combined with the uncertainty in the fluxes used for the calibration, this mostly yields errors $\lesssim 10\%$. The exceptions are the L'- and M'-band images for object C, where the errors are substantially larger.

In Fig. 6 we analyse the NIR colours and magnitudes of the two sources (filled symbols). In addition, we estimated the photospheric colours and magnitudes by comparing the

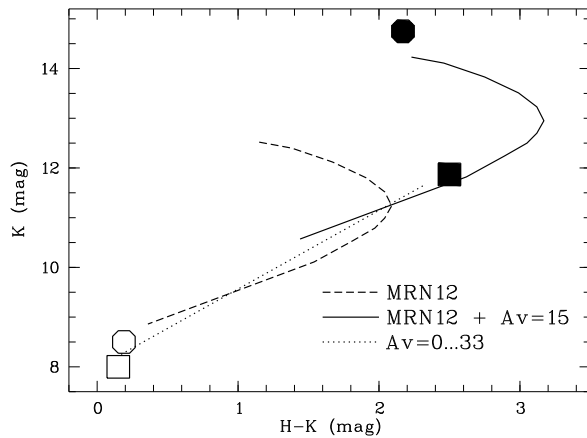


Figure 6. Colour-magnitude diagram illustrating the interpretation of the near-infrared photometry. Filled symbols show measured photometry; empty symbols the approximate photospheric fluxes obtained by comparing the constraints on T_{eff} with the 1 Myr evolutionary track by Baraffe et al. (1998). Squares correspond to object AB and octagons to object C. The dotted line is the reddening path for $A_V = 1 - 33$ with the Mathis (1990) extinction law. The dashed line show the standard scattering model MRN12 from Kenyon et al. (1993b) with inclinations ranging from $\cos i = 0.975 - 0.0$. The solid line is the scattering model plus extinction.

constraints on the effective temperatures with the 1 Myr evolutionary track by Baraffe et al. (1998) (empty symbols). For source C, we used $T_{\text{eff}} = 3400$ K, as derived by comparing the spectrum to models (Sect. 3.2). For object AB we only have a limit on the spectral type (\lesssim early M), which corresponds to $T_{\text{eff}} \gtrsim 3600$ K (Mentuch et al. 2008). Thus, the plotted flux constitutes a lower limit as well. These photospheric datapoints may be uncertain in the y-axis by up to ± 1 mag due to the unknown age and the uncertainty in T_{eff} , but this does not affect the following interpretation significantly.

For object AB (square symbols) the colours are well explained by the extinction path (dotted line), indicating a line

⁴ <http://www.gemini.edu/sciops/instruments/mir/MIRStdFluxes.txt>

of sight extinction of $A_V \sim 30$ mag, in agreement with our constraint from the spectrum (Sect. 3.1). Thus, both spectroscopy and photometry are consistent with an extinguished photosphere of a single low-mass star. For object C (octagons), however, it is clear that extinction alone cannot explain the $H - K$ colour. Object C appears to be 6 mag fainter in the K-band image than expected from the photospheric fluxes derived from the spectrum. Scattered light models provide a much better fit. The solid line shows the model MRN12 from Kenyon et al. (1993b) plus an extinction of $A_V = 15$ mag, which allows to reproduce the K-band flux and the colour simultaneously. This analysis confirms that the object is mostly seen in scattered light through an edge-on disk.

In summary, the information from photometry and spectroscopy indicates that AB and C are both low-mass stars. Since the mass of AB is likely to be higher than the mass of C and AB is located closer to the core of the nebula, AB is probably the most relevant center of infall in the IRAS04325 system.

3.4 PSF fitting

It has been speculated that AB might be a binary (hence the name). Based on the HST images, Hartmann et al. (1999) argue that 'there is a double structure, possibly indicating two sources or possibly indicating a dark absorption lane running roughly east-west across the object.' In the HST images the separation between the two components is in the range of $0''.2$ roughly in north-south direction, corresponding to ~ 30 AU. The 'dark lane' would indicate an absorption feature in front of the object, possibly a disk with diameter of a few tens AU.

Based on our K-band image, we test for the presence of a second source in AB by constructing a model PSF from the three well-detected field stars outside IRAS04325. All sources in the image are fit with this model PSF, using `daophot` within IRAF. The χ^2 of the fit is < 2 for all field stars, 3.2 for object C, and 12.0 for object AB. The contour plot of the residuals (Fig. 7) after subtracting one PSF does not show any evidence for a second point source, and fitting two PSFs instead of one does not improve the fit. The high χ^2 is most likely caused by the strongly uneven background and not by a stellar companion.

Thus, we prefer to interpret the double structure seen in the HST image as an indication for a disk seen at high inclination that bisects the image of the star, rather than the presence of a resolved companion. This finding is supported by the combined information from photometry and spectroscopy; for a binary we would expect a mismatch (i.e. a later spectral type than expected from photometry). The orientation of the 'lane' is roughly perpendicular to the outflow emanating from AB (Sect. 4).

In the submm continuum image both AB and C are spatially resolved. The spatial structure is studied after discarding the data from baselines shorter than 44 m, which effectively removes the structures larger than a few arcsec. We used the task `uvfit` in the Miriad package to fit the visibilities of the sources. Various combinations of point sources and gaussian sources were tried for both objects.

The northern source C is well matched by an elliptical gaussian with axes of $1''.2$ and $0''.2$ and a position angle of

~ 50 deg (Fig. 2). Note that the position angle of the beam is SE to NW, i.e. perpendicular to the orientation of the source. The parameters of the gaussian have large uncertainties, but it is safe to conclude that the position angle is consistent with the orientation of the disk, as inferred from the HST images (PA 30 deg, Hartmann et al. 1999). The same HST images also constrain the radius of the disk to $0''.2$ (~ 30 AU), which is not resolved by the SMA. The elongated structure seen in the submm data might be caused by a cold outer disk or by an elongated circumstellar envelope with a diameter of $\sim 1 - 2''$, i.e. 150-300 AU. This size matches well with the constraint from the SED modeling (Sect. 5.2).

The southern AB source contains a compact component that is well matched by a point source, likely caused by a small-scale disk. In addition there is a contribution of spatially extended emission, mostly oriented in E-W direction over an area of $3-5''$.

3.5 Astrometry

Based on the PSF fit discussed in Sect. 3.4 the relative positions of AB and C were determined with an accuracy in the range of $0''.1$ (1 pixel). The distance between the two sources measured from the peak position of the model PSF is $8''.32$. Simply measuring the positions of the emission peaks also gives a consistent distance of $8''.3$. From the coordinates given by Hartmann et al. (1999), based on images from November 1997, we infer a distance between AB and C of $8''.23$. Within the errorbar both measurements are consistent.⁵ The position angles from the available near-infrared images agree well: We measure 351.8 deg (E of N), while the literature values are 351.4 (Connelley et al. 2008) and 351.6 deg (Hartmann et al. 1999), all with uncertainties of $\lesssim 1$ deg.

These measurements constrain the relative proper motion between AB and C to < 9 mas yr $^{-1}$. For comparison, the average proper motion of young stars within 5 deg of IRAS04325 is 23 mas yr $^{-1}$ (Ducourant et al. 2005; Luhman et al. 2009), with a standard deviation of 10 mas yr $^{-1}$. While the constraints on the proper motion for AB and C do not prove that the object is a physically bound system, they do confirm common membership in the Taurus association.

The angular distance between AB and C correspond to a separation of 1250 AU and a relative movement $\lesssim 15$ AU over 11 yr, which results in an upper velocity limit of 6 kms $^{-1}$ between AB and C. This does not rule out the possibility that C has been much closer to AB in the past: With a velocity of 6 kms $^{-1}$ it would have taken only 10^3 yr for C to move to its current position from a starting point close to AB. It is thus conceivable that C has been ejected by a close dynamical encounter with AB in the early evolution of the system.

⁵ For completeness, the relative distance from the astrometry given by Connelley et al. (2008) based on imaging from 2003-5 is $8''.03$; the accuracy of their astrometry is not clear.

4 MORPHOLOGY OF IRAS04325

4.1 Structure within IRAS04325

The IRAS source is located within the small dark cloud L1535, a part of the B18 cloud complex in Taurus. The few field stars visible in both H- and K-band have $H - K$ colours of 2-3 mag, corresponding to extinctions of 25-35 mag, which indicates substantial amounts of gas and dust along the line-of-sight.

The near- and mid-infrared images of IRAS04325 show a bright elongated emission nebula (Hodapp 1994; Hartmann et al. 1999; Connelley et al. 2007). In our images in the JHK bands the dimensions of this nebulosity are about $10'' \times 20''$, corresponding to 1500×3000 AU, with a position angle (PA) of $\sim 15-20$ deg. The nebula is divided in two lobes. While the northern lobe is brighter, the southern one is more extended with two long light streaks visible up to $15''$ to the south of the nebulosity center. The structure is best explained as light from object AB scattered by dust at the edges of an outflow cavity; indeed, the orientation fits with various outflow related features (Sect. 4.2).

Apart from the two compact sources, the multi-wavelength images reveal a complex substructure in IRAS04325, see the contour plot in Fig. 7, where we have subtracted a point source at the position of AB (see Sect. 3.4). We note that the PSF subtraction affects only the area within $0.5''$ radius of AB and does not alter the structure seen in the figure. There are two extended features in close proximity to AB (Fig. 7, left panel). The southern feature, called D in the following, has a peak $0.7''$ SW of AB and appears in the K-band as a half-ring broadly covering the south part of the point source. This is best explained by scattered light from an envelope around the central source, with a radius of about 100 AU. The position and structure of this feature agrees well with extended CO emission seen in the submm regime at radial velocities of $6.5-8 \text{ km s}^{-1}$, indicating the presence of cold gas. In the CO map the maximum intensity is seen at 6.9 km s^{-1} with a peak at $0.8''$ south of AB (Fig. 3).

The northern feature, called E in the following, appears in the K-band as an open cone with an apex located $1.2''$ north to AB, corresponding to 180 AU (see Fig. 1 and 7). Two curved light streaks extend this structure towards the east and west. The same extensions are seen in the submm continuum image (Fig. 2). The position of feature E also coincides with a CO lobe seen in a velocity regime between 2 and 5 km s^{-1} (see Fig. 3). It is most pronounced at $4-4.5 \text{ km s}^{-1}$, with a peak position at about $1.0''$ north of AB. Feature E is orientated at a position angle of ~ 15 deg with respect to AB, coinciding with the orientation of the emission nebula. The morphology and orientation fit well with an interpretation as part of the outflow cavity.

Our own K-band image and the one from HST (Hartmann et al. 1999) show a faint S-shaped structure connecting the point sources AB and C and extending further to the north (Fig. 1 and 7, right panel). This is most likely scattered light from dust features. It is possible that this 'bridge' between AB and C is coincidental; we see the extension of the outflow-related feature E (see above) and light streaks originating from source C in superposition in the plane of the sky. Hartmann et al. (1999) argued that the two faint features near C are scattered light from the cavity edges of

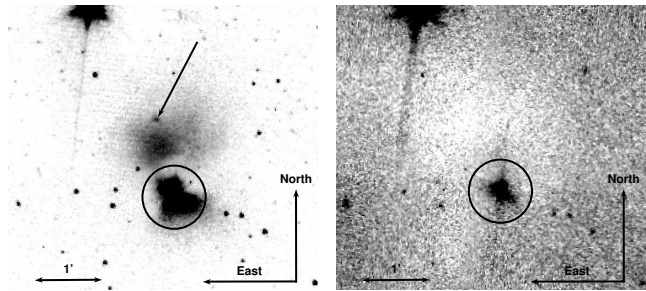


Figure 8. Spitzer IRAC images centered on the nebulosity north of IRAS04325 at 4.5 (left) and $8.0 \mu\text{m}$ (right). IRAS04325 is marked with a black circle. Noteworthy are a) the emission knot seen at $4.5 \mu\text{m}$ (left panel, marked with arrow) at the northern end of the nebula and b) the dark feature visible at $8 \mu\text{m}$.

an outflow from object C. Their direction is $60-90$ deg offset from the orientation of the disk seen in the HST images, which fits into the outflow interpretation. However, in our CO observations there is no evidence for outflow lobes at the same positions (see below).

Therefore we prefer a scenario in which these structures belong to a physical 'bridge' between AB and C. Such a 'bridge' could be indicative of gravitational interaction in the early evolution of the system, but the long-term stability of the outflows (Sect. 4.2) argues against this interpretation. Instead we propose to explain the structure as dust features from interacting accretion streams (as speculated by Hartmann et al. (1999)). The S-shaped morphology indeed resembles the density maps in accreting binaries from the SPH simulations by Bate & Bonnell (1997).

Two CO lobes are detected in close proximity to source C in a narrow velocity range of $6.5-7.5 \text{ km s}^{-1}$ (see Fig. 3). The strongest one is almost exactly coinciding with the position of the compact source seen in the continuum image: the offset between peak of the CO intensity and peak in the continuum is $< 1.0''$. The PA for the elongation of this CO lobe is roughly 300 deg. The second CO blob is located roughly $5''$ away at PA ~ 290 deg with respect to C. A third CO detection is seen in the velocity range of $4.4-4.8 \text{ km s}^{-1}$ $5''$ west of object C at PA of ~ 270 deg. The orientation of these three CO features is roughly perpendicular to the alignment of the disk (PA 30 deg). Thus, they could be associated with an outflow from source C.

4.2 Structure outside IRAS04325

A region of diffuse near-infrared emission is found about $40''$ north and $15''$ east of IRAS04325AB, corresponding to a PA of 20 deg (see Fig. 8). Thus, this area is located in the extension of the axis defined by the elongated emission nebula. The feature has been mentioned before in the literature, for example by Park & Kenyon (2002), and is most pronounced at 2 to $5 \mu\text{m}$. In our K-band image the feature has a size of $20'' \times 20''$. The proximity to IRAS04325 and the location along the outflow axis lead us to believe that the feature is physically associated with IRAS04325. Under this assumption the physical distance from IRAS04325 would be ~ 6000 AU. This patch of emission could be scattered light at the northern end of the outflow cavity.

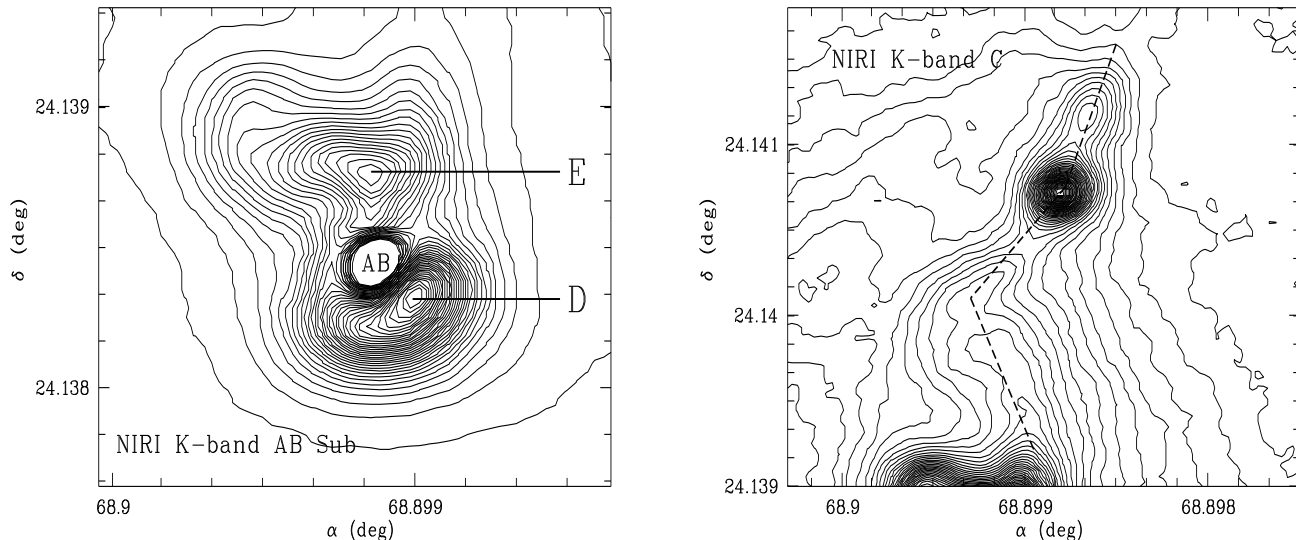


Figure 7. Contour maps of the K-band image from Gemini/NIRI around the source IRAS04325. One small tickmark corresponds to $0''.6$ (5 pixel). The left panel shows a small area around source AB after subtracting one point source centered at the peak of the emission. The total image size is $6'' \times 6''$. The two extended structures D and E to the south and north of the point source are clearly visible. The right panel shows the northern part of the source around object C; image size $10'' \times 10''$. The dashed lines mark the light streaks connecting AB and C and extending further to the north. Note that the dark lane from the disk around C, as seen in the HST image, is not resolved here.

In the IRAC bands at 3.6 and $4.5 \mu\text{m}$ a 10 - $15''$ wide, dark band is visible between the IRAS04325 nebula and the emission region further north (Fig. 8, left panel), possibly a foreground cloud blocking the view to the source.

At $8 \mu\text{m}$ the bright diffuse patch in the north of IRAS04325 is not visible, instead the image shows a roughly circular, $1.5' \times 1.5'$ absorption feature centered $70''$ north and $30''$ east of IRAS04325 (PA 23 deg), i.e. just north of the bright patch (Fig. 8, right panel). This dark feature has fainter extensions to the east and south, overlapping with IRAS04325. Its center is located along the outflow axis of IRAS04325AB. The position agrees well with the core L1535 N-SMM seen in the submm maps of IRAS04325 presented by Hogerheijde & Sandell (2000), indicating that this feature represents an overdensity of dust. It is possible that the northern lobe of the outflow is blocked by this core, explaining the lack of large-scale outflow features further to the NE (see below).

The dark feature is only visible at $8 \mu\text{m}$, and not at any other wavelength in the mid-infrared. In the $8 \mu\text{m}$ image it is the only such feature within a radius of one degree. This may be related to the presence of strong PAH emission bands in the other IRAC bands (e.g. Peeters et al. 2002). It is conceivable that we see a region of strong absorption projected against the bright PAH background, as they are often found in the Galactic plane (e.g. Egan et al. 1998). In fact, the combination of submm emission and $8 \mu\text{m}$ absorption has been observed for a number of cores in infrared dark clouds (Vasyunina et al. 2009).

IRAS04325+2402 has long been known to drive molecular outflows (Heyer et al. 1987; Terebey et al. 1989; Moriarty-Schieven et al. 1992). Specifically, a large body of evidence is available for an outflow driven by source AB at position angle of 10 - 20 deg. Features associated with this outflow are the elongated emission nebula (also seen in

HCO^+ , Hogerheijde et al. 1998), the scattered light feature E (Sect. 4.1), the HH objects 434-436 about 1 deg southwest (2.7 pc) of the IRAS source at PA of 17.5 - 19.5 deg (Wang et al. 2001), and HH703 $30'$ south of IRAS04325 (1.4 pc) at PA of 16 deg (Sun et al. 2003)

We searched in the H_2 images as well as in the IRAC images for more shock features along the outflow axis. In particular the IRAC band 2 ($4.5 \mu\text{m}$) is known to contain a number of bright emission lines of shocked H_2 (see Ybarra & Lada 2009, and references therein). The group of Herbig-Haro objects 434-436, so far only detected in the [SII] line and possibly part of a bow shock (Wang et al. 2001), is well-visible in H_2 and in all four IRAC bands. In the $4.5 \mu\text{m}$ image we find an additional knot about $1.1'$ north of AB (10000 AU) at PA 14 deg (α $4^{\text{h}}35^{\text{m}}36^{\text{s}}.5$, δ $+24^{\circ}09'25''.5$ (J2000), Fig. 8, left panel). This feature is clearly extended and not seen at any other wavelength, which argues for an association with the outflow. No other obvious feature was found for PA of 15 - 20 deg and separation from IRAS04325 up to 1 deg in both directions.

There is a second large-scale outflow emanating from IRAS04325+2402, identified by Heyer et al. (1987). The outflow is seen in integrated CO emission spanning $12'$, i.e. 0.5 pc if related to IRAS04325. It is described as well-collimated, redshifted, and monopolar. In clear disagreement to the first outflow discussed above, this second flow is oriented from the IRAS source towards the NW at position angle around ~ 310 deg, roughly perpendicular to the disk of source C.

The most likely source for this second outflow is object C. This star clearly has jet activity, proven by the variety of outflow related emission lines in the near-infrared spectrum. Three CO lobes are seen around this object with PA of 270 - 300 deg, roughly matching the orientation reported by Heyer et al. (1987), which could belong to the outflow

as well. We do not find any additional counterparts of this outflow in the H₂ and the IRAC images.

5 SED MODELING

We aim to reproduce the spectral energy distributions (SED) for objects AB and C with a Monte Carlo radiative transfer code. In addition to the data presented here and in Scholz et al. (2008) we make use of the Spitzer/IRS spectrum available for object AB (Furlan et al. 2008). Only the SL exposure is used, which is obtained through a 3''6 wide slit oriented roughly in N-S direction and covers the wavelength range from 5.2 to 14 μm. This spectrum matches well with the photometry at 11.2 μm. We do not use the LL spectrum (obtained through a 10''6 slit) and the IRAC/MIPS photometry, due to their poor spatial resolution.

Our model code computes thermal radiation and non-spherical scattering from dust in a two-dimensional axisymmetric system with central source, flared disk, and larger-scale flattened envelope with a narrow evacuated bipolar outflow cavity (e.g. Whitney et al. 2003b,a). The central photospheres are approximated with NextGen model atmospheres (Hauschildt et al. 1999; Allard et al. 2001) with $\log g = 4$. The main free parameters for the disk are mass, outer radius, inner radius, accretion rate, scale height factor h_0 and flaring power β . The latter two are defined as $h = h_0(r/R_*)^\beta$, with h the scaleheight of the disk and r the distance from the star. The parameters for the envelope include envelope accretion rate, mass, outer radius, and outflow cavity angle. In addition the model fits the ambient density and the interstellar extinction between the source and the observer.

For the envelope we assume dust with an interstellar-like size distribution, using the model by Kim et al. (1994). In the disk we use a dust model including silicates and carbonaceous grains with solar abundances. Here the grain size distribution is a power law with an exponential decay for particles with sizes above 50 μm and a formal maximum grain size of 1 mm (Wood et al. 2002). This dust model thus allows for the presence of larger grains than in the ISM. For more details and references about the radiation transfer code see Scholz et al. (2006) and Robitaille et al. (2006). The code has recently been extended to treat the non-thermal reprocessing of photons by PAH molecules and very small grains (VSG, Wood et al. 2008), using opacities, abundances, and re-emission templates from Draine & Li (2007).

Given the large number of free parameters and the numerous simplifying assumptions (e.g., two-dimensional disk, axisymmetric system, no variability), the modeling is subject to degeneracies (e.g. Chiang et al. 2001; Robitaille et al. 2007). The models presented here are by-eye fits to the SED and do not represent a unique solution. We do not claim to have explored the full parameter space. Instead, we use the model to verify if the SEDs can in principle be understood in the commonly used framework of disk/envelope models. In addition, this will provide an independent test for the plausibility of the constraints for the physical parameters of the system. The parameter best constrained by the modeling are the circumstellar mass, as it depends only on the submm/mm datapoints. On the other hand, the mass dis-

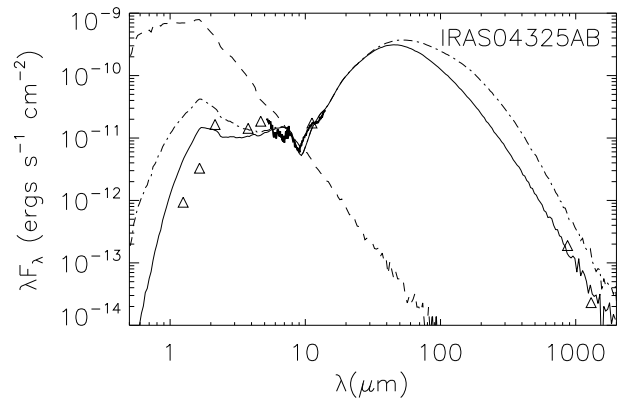


Figure 9. SED fitting for IRAS04325AB. Shown with solid line is a model calculated for a square aperture of 200 AU, i.e. comparable to the observations. The dash-dotted line shows the same model for the full scale of the simulation (10⁵ AU). The photospheric spectrum is plotted as dashed line. The observed fluxes are plotted with triangles, except for the IRS spectrum, which is seen as a thick solid line between 5 and 14 μm. The models assume an external (i.e. outside disk and envelope) extinction of $A_V = 3$ mag.

tribution in disk and envelope, the disk inclination, as well as the extinction are poorly constrained.

5.1 Object AB

Figure 9 shows a model for object AB computed without the inclusion of PAH/VSGs. We find that the two-dimensional model with disk, envelope, and outflow cavity is able to reproduce many of the features of the observed SED. One matching SED model is shown in Fig. 9. This specific model is based on the following parameters, consistent with the observational constraints: stellar mass 1 M_\odot , stellar radius 2 R_\odot , effective temperature 3800 K, disk inclination 78 deg, disk mass 10⁻³ M_\odot , disk radius 50 AU, disk accretion rate 10⁻⁸ M_\odot yr⁻¹, scale height factor 0.01 R_* , flaring power 1.25, envelope accretion rate 3 · 10⁻⁶ M_\odot yr⁻¹, cavity half opening angle 10 deg. The total circumstellar mass is 0.18 M_\odot for the full scale of the simulation of 10⁴ AU.

These results are consistent with previous attempts to model the source. For example, Whitney et al. (1997) find a centrifugal disk radius of 50 AU, an inclination of 72-90 deg, and a total infall rate of 5 · 10⁻⁶ M_\odot yr⁻¹ based on near-infrared imaging polarimetry. The model presented by Furlan et al. (2008) aims to reproduce the full IRS spectrum and broadband photometry from the near-infrared to the mm regime and results in a centrifugal disk radius of 100 AU, a cavity semiopening angle of 15 deg, and a disk inclination angle of 80 deg.

The largest discrepancies between model and observed SED occur in the near- and mid-IR. This part of the SED is sensitive to small changes in extinction, stellar parameters, disk inclination and to non-axisymmetric geometries (Indebetouw et al. 2006). The images of this object show a complex geometry, i.e. 3D effects will likely affect the mid-IR emission.

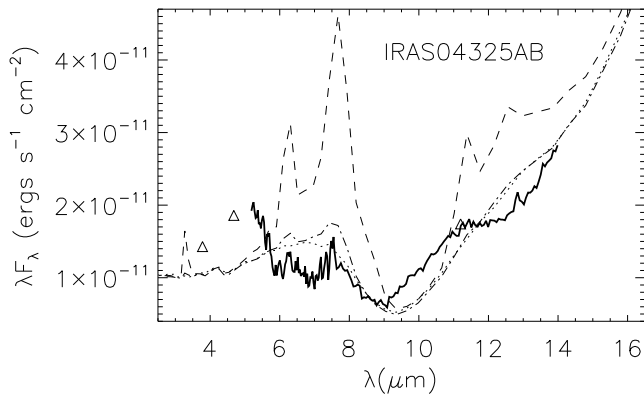


Figure 10. Modeling the IRS spectrum (solid line) for IRAS04325AB. The dotted line is a model without PAH, i.e. the same as in Fig. 9. For the dash-dotted line model, we include PAH in the disk. The dashed line has PAH in the disk and envelope. Triangles show the photometric datapoints. All models are calculated using the same parameters as in Fig. 9. They assume an external (i.e. outside disk and envelope) extinction of $A_V = 3$ mag.

The IRS spectrum for this object, shown in detail in Fig. 10, is not well-reproduced by our model. The deep absorption trough around $9 \mu\text{m}$ is most likely caused by the amorphous silicate absorption band at $9.7 \mu\text{m}$, as seen in many other protostars (Furlan et al. 2008). In addition, the spectrum could be affected by the frequently observed ice absorption bands at 6.0 and $6.8 \mu\text{m}$ (e.g. van Dishoeck 2004).

On the other hand, the peaks at 6.2 and $7.6 \mu\text{m}$ coincide with two of the most prominent features of PAH emission spectra (Peeters et al. 2002). We made an attempt to model the spectrum by including treatment of PAH/VSGs in the radiative transfer simulations. In Fig. 10 we show the model with PAH only in the disk (dash-dotted line) as well as PAH in disk and envelope (dashed line). Qualitatively the shape of the two peaks is matched by the model. The absolute flux levels, however, are not adequately reproduced by these PAH models. The strength of the peaks is highly sensitive to the location of the PAH; in this case, a model with PAH only in the disk provides the best match.

PAH emission is generally found to be rare in disks around young stellar objects, particularly in late-type objects (Geers et al. 2006; Furlan et al. 2006), with detection rates below 10%. Given the rarity of PAH features and the ubiquity of ice features in low-mass protostars, we consider it more likely that ices are predominantly responsible for the shape of the mid-infrared spectrum in IRAS04325AB. As our analysis has shown, the presence of PAH provides an alternative plausible interpretation for the peaks. To disentangle these effects, it is necessary to include ice opacities in the models, see for example Crapsi et al. (2008).

5.2 Object C

In Fig. 11 we show the SED for object C and a model SED that matches most of the datapoints. In the modeling we fix the effective temperature of the central object (3400 K , see

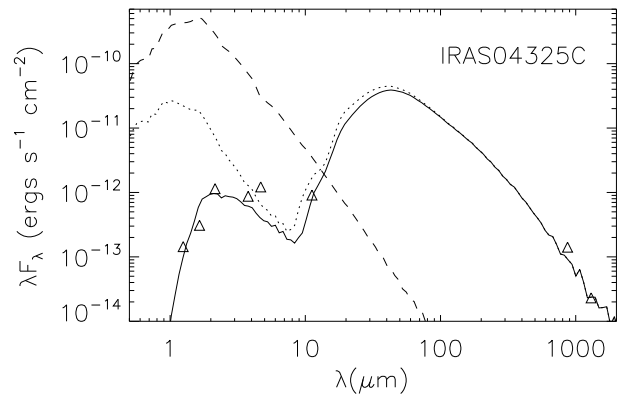


Figure 11. SED fitting for IRAS04325C. Shown is a model with $A_V = 17.5$ mag that matches all available independent constraints (effective temperature, disk radius, accretion rate). Note that the J-band flux is an upper limit. The dashed line shows the photospheric spectrum, the dotted line the intrinsic SED without external extinction.

Sect. 3.2), the accretion rate ($10^{-8} M_\odot \text{ yr}^{-1}$, see Sect. 3.2), and the outer disk radius (30 AU, Hartmann et al. 1999). In addition, we require a high disk inclination ($i > 80$ deg). An edge-on or close to edge-on geometry is necessary to reproduce the appearance of the HST image and to explain why photometry and spectroscopy cannot be simultaneously reproduced by an extinguished photosphere (see Sect. 3.3).

The model shown in Fig. 11 is calculated for $R_* = 1.8 R_\odot$, $i = 85$ deg, $h_0 = 0.01 R_*$, $\beta = 1.25$, i.e. the disk is assumed to be affected by relatively strong flaring. The total mass in disk and envelope has to be between 0.001 and $0.01 M_\odot$ to reproduce the submm/mm datapoints (assuming the canonical gas-to-dust ratio of 100). The model predicts most of the circumstellar mass to be in the disk ($0.004 M_\odot$), with only a thin envelope ($6 \cdot 10^{-5} M_\odot$), but other configurations are conceivable. The envelope has an outer radius of 300 AU , an accretion rate of $10^{-7} M_\odot \text{ yr}^{-1}$, and an outflow cavity with half-opening angle of 15 deg.

The model assumes interstellar extinction of $A_V = 17.5$ mag. This does not include the extinction caused by disk and envelope, which is extremely high for this object due to the edge-on disk. The value for the extinction agrees well with the estimate we obtain from the combined information of near-infrared spectroscopy and photometry (Sect. 3.3). It differs significantly from the extinction used in the SED modeling for object AB ($A_V = 3$ mag, Sect. 5.1), which is implausible because outside the disk/envelope systems the extinction should be comparable. As noted before, the constraint for A_V obtained from SED modeling is subject to large uncertainties, due to the numerous degeneracies in the near-infrared SED.

As seen in Fig. 11, the photometric datapoint in the M'-band at $4.7 \mu\text{m}$ is difficult to reproduce with these models. This does not depend on the particular choice of disk/envelope properties; the datapoint is an outlier for all reasonable combinations of parameters. Most models predict a decreasing SED (in λF_λ) between 3 and $5 \mu\text{m}$, whereas the datapoint at $4.7 \mu\text{m}$ is 30% higher than the one at $3.6 \mu\text{m}$.

One possible explanation is additional flux generated by the outflow, which is not part of the model. The M'-band contains a number of strong H_2 emission lines typical for shocks in protostellar outflows (Ybarra & Lada 2009), in particular the 0-0 S(9) transition at $4.69 \mu\text{m}$. Shocked H_2 emission, as seen in the near-infrared for this object (Sect. 3.2), could contribute significantly to the M'-band flux.

6 SUMMARY AND CONCLUSIONS

We present a multi-wavelength study for the embedded protostellar system IRAS04325+2403. IRAS04325 is one of very few known multiple YSOs with at least one resolved disk and two protostellar jets. New imaging with subarcsecond resolution has been obtained in the infrared covering the wavelength range $1\text{-}12 \mu\text{m}$ and in the sub-millimetre at $870 \mu\text{m}$. This is combined with low-resolution near-infrared spectroscopy for the two compact sources in the system and with literature data. In the following we summarize the constraints on the properties of IRAS04325:

(i) We show that the both components in the system are low-mass stars. Object C is an M dwarf, probably with an effective temperature around 3400 K, while AB is likely of earlier type and more massive. Object C is unlikely to be a brown dwarf, as speculated previously.

(ii) Despite the wealth of available data, there are enormous difficulties in estimating the fundamental parameters of the central sources. In particular, the presence of veiling, disks, and strong line-of-sight extinction puts limits on our ability to reliably derive effective temperatures from spectra. The poorly constrained age hampers the conversion to masses.

(iii) The near-infrared emission line spectrum for object C provides strong evidence for ongoing accretion and jet activity.

(iv) We argue that the previously seen double structure of object AB is not due to the presence of a close stellar companion. Instead it is best explained by an absorption lane in front of the object, most likely caused by a disk.

(v) Comparing our astrometry with the positions reported by Hartmann et al. (1999), we put a limit of $< 9 \text{ mas yr}^{-1}$ on the relative proper motion between AB and C. This confirms common membership in the Taurus star forming region.

(vi) The morphology and SED for object AB is consistent with the presence of a small disk (radii $\sim 50 \text{ AU}$ radius) and a larger envelope ($\lesssim 100 \text{ AU}$ radius).

(vii) Object C has been found to have an edge-on disk with radius 30 AU by Hartmann et al. (1999). Our observations confirm that the object is mostly seen in scattered light due to the high inclination. Based on submm imaging and SED analysis we identify an elongated envelope or outer disk with radius of $\lesssim 300 \text{ AU}$ around this object.

(viii) The mass of circumstellar material in the system is well-constrained by the submm/mm datapoints. While the disk masses are quite small ($0.001\text{-}0.01 M_\odot$), the total mass within 10000 AU is in the range of $0.2 M_\odot$.

(ix) Many of the features in the SED and the multi-wavelength images can be understood in the framework of commonly used two-dimensional disk and envelope models. The remaining inconsistencies may well be caused by the

3D structure of the system, which is visible in the images but not accounted for in the models. The mid-infrared spectrum for source AB shows spectral features that cannot be matched with a standard model using a single population of dust grains; instead they require the inclusion of silicates, ices, and possibly PAHs.

(x) We identify several new features associated with a parsec-scale outflow driven by object AB with position angle of $10\text{-}20 \text{ deg}$. Object C likely has its own large-scale outflow at position angle of $270\text{-}310 \text{ deg}$.

(xi) Various pieces of evidence indicate an early evolutionary state for IRAS04325. The star-disk systems are embedded in a core with a large line-of-sight extinction of $A_V \sim 30 \text{ mag}$. The object is undetected in the Taurus XMM X-ray survey (Güdel et al. 2007), which is unusual for Class II objects (15% undetected), but common for protostars (60%). The bolometric luminosity of the system, as determined by fitting the unresolved SED (Froeblich 2005), is around $1.0 L_\odot$. According to the pre-main sequence tracks by D'Antona & Mazzitelli (1994, update 1998), two objects with effective temperatures around 3400 K would have a total luminosity of 1.3, 1.0, $0.9 L_\odot$ at 10^5 , 2×10^5 , and $5 \times 10^5 \text{ yr}$. Thus, an age of a few times 10^5 yr seems reasonable.

(xii) The position angles of disks, envelopes, and outflows put useful limits on the geometry of the system. For the AB disk/envelope, C disk/envelope, and binary orbit the position angles are approximately 90, 30, and 350 deg. Thus, the disk/envelope systems in IRAS04325 are strongly misaligned with respect to each other (60 deg) as well as with respect to the orbital plane of the binary (80 and 40 deg). The disks are neither aligned nor coplanar.

The last finding, first stated by Hartmann et al. (1999) and bolstered here by more evidence, warrants some further comments. From polarimetry studies it is known that the dominant majority (80-90%) of young binaries has disk orientations within 30 deg of the orbital plane (Jensen et al. 2004; Monin et al. 2006). There are exceptions, found by imaging the jets (e.g. Davis et al. 1994; Lim & Takakuwa 2006) or disks (Kang et al. 2008), but many of them seem to be higher-order systems where one of the components is again a close binary (see the review by Monin et al. 2007). This could be the case for IRAS04325 as well, although we argue against the presence of an additional component.

Misalignments can be either primordial or arise during the early evolution, due to dynamical interactions in a multiple system. In the case of IRAS04325 the presence of parsec-scale outflows with constant directions to within a few degrees seems to exclude strong alignment changes in the recent history. Typical dynamical timescales for parsec-scale jets are 10^4 yr (e.g. Eislöffel & Mundt 1997). For the NS jet driven by object AB we estimate a lifetime of $10^4 - 10^5 \text{ yr}$, assuming typical velocities on the order of a few 100 km s^{-1} . The dynamical timescale for the NW jet has been determined to be $2 \times 10^5 \text{ yr}$ (Heyer et al. 1987). Thus the system has been stable over a substantial fraction of its early history. This is confirmed by the absence of strong relative motion between the two components, as it might be expected after recent gravitational encounters.

In general the misalignments between disks and orbits in binary systems will decay with time; the timescale

for this readjustment is expected to be in the order of 20 orbital periods or 10^6 yr for IRAS04325 (Bate et al. 2000; Jensen et al. 2004), which might be longer than its lifetime. For higher-order systems the timescales for realignment are much longer, because the various orbital planes have to be realigned, not only the disks. In addition, the disk radii in IRAS04325 are significantly smaller than the orbital separation (< 50 AU vs. 1250 AU). In such cases it is possible that the tilt between disks and orbital plane grows with time and an initial misalignment is enhanced (Lubow & Ogilvie 2000). Thus, IRAS04325 might be a good case for a system where we see primordial misalignment between disks and orbital plane.

For a wide, isolated system like IRAS04325+2402 there are two main possible avenues of formation: fragmentation from a centrifugally supported core (rotational fragmentation) or from turbulent material (turbulent fragmentation) – see Goodwin et al. (2007) for a review. As discussed extensively by Bate et al. (2000), primordial misalignments are easy to produce in a turbulent fragmentation scenario, for example due to spatial variations in the direction of angular momentum within the core. On the other hand, rotational fragmentation predicts a strong alignment between disks and orbit. The picture presented here for IRAS04325 shows that strong misalignments can be present even in small-scale star forming environments and favours turbulent fragmentation as the formation scenario.

ACKNOWLEDGMENTS

We thank Ian Bonnell for instructive discussions related to subjects discussed in this paper and Dirk Froebrich for pointing us to the publicly available H_2 images for this region. We received the IRS spectrum from Elise Furlan who also gave helpful comments on an early version of the paper. Her help is greatly appreciated. The careful and constructive review by the anonymous referee helped to improve the paper significantly. AS would like to acknowledge financial support from the Scottish Universities of Physics Alliance SUPA under travel grant APA1-AS110X. ACG acknowledges financial support from the Science Foundation Ireland, grant 07/RFP/PHYF790.

REFERENCES

- Allard F., Hauschildt P. H., Alexander D. R., Tamanai A., Schweitzer A., 2001, *ApJ*, 556, 357
- Baraffe I., Chabrier G., Allard F., Hauschildt P. H., 1998, *A&A*, 337, 403
- Bate M. R., Bonnell I. A., 1997, *MNRAS*, 285, 33
- Bate M. R., Bonnell I. A., Clarke C. J., Lubow S. H., Ogilvie G. I., Pringle J. E., Tout C. A., 2000, *MNRAS*, 317, 773
- Bertin E., 2006, in *Astronomical Society of the Pacific Conference Series*, Vol. 351, *Astronomical Data Analysis Software and Systems XV*, C. Gabriel, C. Arviset, D. Ponz, & S. Enrique, ed., pp. 112–+
- Bertin E., Mellier Y., Radovich M., Missonnier G., Didelon P., Morin B., 2002, in *Astronomical Society of the Pacific Conference Series*, Vol. 281, *Astronomical Data Analysis Software and Systems XI*, D. A. Bohlender, D. Durand, & T. H. Handley, ed., pp. 228–+
- Brandeker A., Jayawardhana R., Ivanov V. D., Kurtev R., 2006, *ApJ*, 653, L61
- Bryson I. R., Glasse A. C., Atad-Ettedgui E. I., 1994, in *Presented at the Society of Photo-Optical Instrumentation Engineers (SPIE) Conference*, Vol. 2198, *Society of Photo-Optical Instrumentation Engineers (SPIE) Conference Series*, D. L. Crawford & E. R. Craine, ed., pp. 715–724
- Calvet N., Muzerolle J., Briceño C., Hernández J., Hartmann L., Saucedo J. L., Gordon K. D., 2004, *AJ*, 128, 1294
- Chiang E. I., Joungh M. K., Creech-Eakman M. J., Qi C., Kessler J. E., Blake G. A., van Dishoeck E. F., 2001, *ApJ*, 547, 1077
- Cohen M., Walker R. G., Carter B., Hammersley P., Kidger M., Noguchi K., 1999, *AJ*, 117, 1864
- Connelley M. S., Reipurth B., Tokunaga A. T., 2007, *AJ*, 133, 1528
- , 2008, *AJ*, 135, 2496
- Crapsi A., van Dishoeck E. F., Hogerheijde M. R., Pontoppidan K. M., Dullemond C. P., 2008, *A&A*, 486, 245
- Cushing M. C., Rayner J. T., Vacca W. D., 2005, *ApJ*, 623, 1115
- D’Antona F., Mazzitelli I., 1994, *ApJS*, 90, 467
- Davis C. J., Mundt R., Eisloffel J., 1994, *ApJ*, 437, L55
- Davis C. J., Scholz P., Lucas P., Smith M. D., Adamson A., 2008, *MNRAS*, 387, 954
- Devillard N., 1997, *The Messenger*, 87, 19
- Draine B. T., Li A., 2007, *ApJ*, 657, 810
- Ducourant C., Teixeira R., Périé J. P., Lecampion J. F., Guibert J., Sartori M. J., 2005, *A&A*, 438, 769
- Egan M. P., Shipman R. F., Price S. D., Carey S. J., Clark F. O., Cohen M., 1998, *ApJ*, 494, L199+
- Eisloffel J., Mundt R., 1997, *AJ*, 114, 280
- Folja D. F. M., Emerson J. P., 1999, *A&A*, 352, 517
- Froebrich D., 2005, *ApJS*, 156, 169
- Furlan E., Hartmann L., Calvet N., D’Alessio P., Franco-Hernández R., Forrest W. J., Watson D. M., Uchida K. I., Sargent B., Green J. D., Keller L. D., Herter T. L., 2006, *ApJS*, 165, 568
- Furlan E., McClure M., Calvet N., Hartmann L., D’Alessio P., Forrest W. J., Watson D. M., Uchida K. I., Sargent B., Green J. D., Herter T. L., 2008, *ApJS*, 176, 184
- Garcia Lopez R., Nisini B., Giannini T., Eisloffel J., Bacciotti F., Podio L., 2008, *A&A*, 487, 1019
- Geers V. C., Augereau J., Pontoppidan K. M., Dullemond C. P., Visser R., Kessler-Silacci J. E., Evans II N. J., van Dishoeck E. F., Blake G. A., Boogert A. C. A., Brown J. M., Lahuis F., Merín B., 2006, *A&A*, 459, 545
- Goldsmith P. F., Sernyak Jr. M. J., 1984, *ApJ*, 283, 140
- Goodwin S. P., Kroupa P., Goodman A., Burkert A., 2007, in *Protostars and Planets V*, B. Reipurth, D. Jewitt, & K. Keil, ed., pp. 133–147
- Güdel M., Briggs K. R., Arzner K., Audard M., Bouvier J., Feigelson E. D., Franciosini E., Glauser A., Grosso N., Micela G., Monin J., Montmerle T., Padgett D. L., Palla F., Pillitteri I., Rebull L., Scelsi L., Silva B., Skinner S. L., Stelzer B., Telleschi A., 2007, *A&A*, 468, 353
- Hartmann L., Calvet N., Allen L., Chen H., Jayawardhana R., 1999, *AJ*, 118, 1784

- Hauschildt P. H., Allard F., Baron E., 1999, *ApJ*, 512, 377
- Heyer M. H., Snell R. L., Goldsmith P. F., Myers P. C., 1987, *ApJ*, 321, 370
- Hodapp K., 1994, *ApJS*, 94, 615
- Hodapp K. W., Jensen J. B., Irwin E. M., Yamada H., Chung R., Fletcher K., Robertson L., Hora J. L., Simons D. A., Mays W., Nolan R., Bec M., Merrill M., Fowler A. M., 2003, *PASP*, 115, 1388
- Hogerheijde M. R., Sandell G., 2000, *ApJ*, 534, 880
- Hogerheijde M. R., van Dishoeck E. F., Blake G. A., van Langevelde H. J., 1998, *ApJ*, 502, 315
- Indebetouw R., Whitney B. A., Johnson K. E., Wood K., 2006, *ApJ*, 636, 362
- Jensen E. L. N., Mathieu R. D., Donar A. X., Dullaghan A., 2004, *ApJ*, 600, 789
- Kang M., Choi M., Ho P. T. P., Lee Y., 2008, *ApJ*, 683, 267
- Kenyon S. J., Calvet N., Hartmann L., 1993a, *ApJ*, 414, 676
- Kenyon S. J., Whitney B. A., Gomez M., Hartmann L., 1993b, *ApJ*, 414, 773
- Kim S.-H., Martin P. G., Hendry P. D., 1994, *ApJ*, 422, 164
- Kirkpatrick J. D., Barman T. S., Burgasser A. J., McGovern M. R., McLean I. S., Tinney C. G., Lowrance P. J., 2006, *ApJ*, 639, 1120
- Ladd E. F., Adams F. C., Fuller G. A., Myers P. C., Casey S., Davidson J. A., Harper D. A., Padman R., 1991, *ApJ*, 382, 555
- Leggett S. K., Hawarden T. G., Currie M. J., Adamson A. J., Carroll T. C., Kerr T. H., Kuhn O. P., Seigar M. S., Varricatt W. P., Wold T., 2003, *MNRAS*, 345, 144
- Lim J., Takakuwa S., 2006, *ApJ*, 653, 425
- Loinard L., Torres R. M., Mioduszewski A. J., Rodríguez L. F., González-Lópezlira R. A., Lachaume R., Vázquez V., González E., 2007, *ApJ*, 671, 546
- Lubow S. H., Ogilvie G. I., 2000, *ApJ*, 538, 326
- Luhman K. L., Mamajek E. E., Allen P. R., Cruz K. L., 2009, *ApJ*, 703, 399
- Lynds B. T., 1962, *ApJS*, 7, 1
- Mathis J. S., 1990, *ARA&A*, 28, 37
- Mentuch E., Brandeker A., van Kerkwijk M. H., Jayawardhana R., Hauschildt P. H., 2008, *ApJ*, 689, 1127
- Mohanty S., Jayawardhana R., Basri G., 2005, *ApJ*, 626, 498
- Monin J., Clarke C. J., Prato L., McCabe C., 2007, in *Protostars and Planets V*, B. Reipurth, D. Jewitt, & K. Keil, ed., pp. 395–409
- Monin J., Ménard F., Peretto N., 2006, *A&A*, 446, 201
- Moriarty-Schieven G. H., Wannier P. G., Tamura M., Keene J., 1992, *ApJ*, 400, 260
- Morwood A., 1997, *The Messenger*, 88, 11
- Muzerolle J., Hartmann L., Calvet N., 1998, *AJ*, 116, 2965
- Natta A., Testi L., Randich S., 2006, *A&A*, 452, 245
- Nisini B., Caratti o Garatti A., Giannini T., Lorenzetti D., 2002, *A&A*, 393, 1035
- Ohashi N., Hayashi M., Kawabe R., Ishiguro M., 1996, *ApJ*, 466, 317
- Park S., Kenyon S. J., 2002, *AJ*, 123, 3370
- Parker N. D., 1988, *MNRAS*, 235, 139
- , 1991, *MNRAS*, 251, 63
- Peeters E., Hony S., Van Kerckhoven C., Tielens A. G. G. M., Allamandola L. J., Hudgins D. M., Bauschlicher C. W., 2002, *A&A*, 390, 1089
- Rayner J. T., Cushing M. C., Vacca W. D., 2009, *ArXiv e-prints*
- Robitaille T. P., Whitney B. A., Indebetouw R., Wood K., 2007, *ApJS*, 169, 328
- Robitaille T. P., Whitney B. A., Indebetouw R., Wood K., Denzmore P., 2006, *ApJS*, 167, 256
- Saraceno P., Andre P., Ceccarelli C., Griffin M., Molinari S., 1996, *A&A*, 309, 827
- Scholz A., Geers V., Jayawardhana R., Fissel L., Lee E., Lafreniere D., Tamura M., 2009, *ApJ*, 702, 805
- Scholz A., Jayawardhana R., Wood K., 2006, *ApJ*, 645, 1498
- Scholz A., Jayawardhana R., Wood K., Lafrenière D., Schreyer K., Doyon R., 2008, *ApJ*, 681, L29
- Sun K., Yang J., Luo S., Wang M., Deng L., Zhou X., Chen J., 2003, *Chinese Journal of Astronomy and Astrophysics*, 3, 458
- Takami M., Chrysostomou A., Ray T. P., Davis C. J., Dent W. R. F., Bailey J., Tamura M., Terada H., Pyo T. S., 2006, *ApJ*, 641, 357
- Terebey S., Vogel S. N., Myers P. C., 1989, *ApJ*, 340, 472
- Ungerechts H., Winnewisser G., Walmsley C. M., 1982, *A&A*, 111, 339
- van Dishoeck E. F., 2004, *ARA&A*, 42, 119
- Vasyunina T., Linz H., Henning T., Stecklum B., Klose S., Nyman L., 2009, *A&A*, 499, 149
- Wang H., Yang J., Wang M., Deng L., Yan J., Chen J., 2001, *AJ*, 121, 1551
- Watson A. M., Stapelfeldt K. R., Wood K., Ménard F., 2007, in *Protostars and Planets V*, Reipurth B., Jewitt D., Keil K., eds., pp. 523–538
- Whitney B. A., Kenyon S. J., Gomez M., 1997, *ApJ*, 485, 703
- Whitney B. A., Wood K., Bjorkman J. E., Cohen M., 2003a, *ApJ*, 598, 1079
- Whitney B. A., Wood K., Bjorkman J. E., Wolff M. J., 2003b, *ApJ*, 591, 1049
- Wood K., Whitney B. A., Robitaille T., Draine B. T., 2008, *ApJ*, 688, 1118
- Wood K., Wolff M. J., Bjorkman J. E., Whitney B., 2002, *ApJ*, 564, 887
- Ybarra J. E., Lada E. A., 2009, *ApJ*, 695, L120

